Enhanced Photoluminescence Features of Rare Earth Phenylphosphonate Hybrid Nanostructures Synthesized under Nonaqueous Conditions

Weihua Di,*,†,‡ Rute A. S. Ferreira,§ Marc-Georg Willinger,† Xinguang Ren,‡ and Nicola Pinna*,†,‖

Department of Chemistry, CICECO, University of Aveiro, 3810-193 Aveiro, Portugal, Key Laboratory of Excited-state Processes, Changchun Institute of Optics, Fine Mechanics and Physics, Chinese Academy of Sciences, Changchun 130033, People's Republic of China, Department of Physics, CICECO, University of Aveiro, 3810-193 Aveiro, Portugal, and World Class University (WCU) program of Chemical Convergence for Energy & Environment (C2E2), School of Chemical and Biological Engineering, College of Engineering, Seoul National University (SNU), Seoul 151-744, Korea

Received: December 12, 2009; Revised Manuscript Received: February 19, 2010

A novel nonaqueous route was applied for the synthesis of rare earth phenylphosphonate hybrid nanostructures by reacting rare earth chlorides with phenylphosphonic acid in benzyl alcohol. Powder X-ray diffraction and transmission electron microscopy studies reveal the ordered lamellar structure, with an interlayer distance of 1.55 nm. The rare earth phosphate layers are spaced by phenyl rings, which connect the hybrid structure by $\pi-\pi$ interactions. The composition, thermal behavior, and surface state were investigated. It was found that the obtained hybrid materials are multiwavelength emitters due to the overlap of the UV/blue phenyl-related emission with the intra-$4f^N$ emission in the red and green for the Eu^{3+}- and Tb^{3+}-doped hybrids, respectively. We demonstrate that the phenylphosphonate hybrid nanostructures synthesized under nonaqueous conditions constitute a good host for lanthanide ions (Ln^{3+}) in terms of an efficient ligand-to-Ln^{3+} sensitization. For the case of the Eu^{3+}-based hybrids, we also provide evidence that the nonaqueous synthesis route leads to the absence of water molecules within the first coordination sphere of Ln^{3+} and, hence, to a significant increase of the absolute emission quantum yield (0.45) compared with those synthesized by the aqueous route (0.25). This work demonstrates the potential and advantage of nonaqueous routes for the synthesis of organic–inorganic hybrids, specifically, with respect to enhanced photoluminescent features.

Introduction

The concept of organic–inorganic hybrids emerged in the last three decades, with the advent of "soft" inorganic chemistry processes and, in particular, of the sol–gel route.[1,2] The unique characteristics of this versatile process permit the synthesis of multifunctional organic–inorganic hybrid structures, through a "bottom-up" approach based on a tailored assembly at the nanoscale of organic and inorganic building blocks.[3–7]

Organic–inorganic hybrids are multifunctional materials offering a large variety of physical properties, which depend not only on both the inorganic and the organic components but also on the interface between the two counterparts.[8,9] Furthermore, the two components can be easily modified in order to precisely tune the global properties of the final material.[10]

Metal phosphonates are organic–inorganic hybrid materials in which the phosphate and organic layers are arranged alternately with each other to form the ordered lamellar nanostructure.[11–13] The wide choice of metals and the versatility of organophosphorus molecules suggested the possibility of a rational design of structures. The original research of metal phosphonate was directed toward the tetravalent metal cations in the early 1980s,[14–16] subsequently toward di- and trivalent metal cations in the later years.[17,18] The interest in these hybrids

originated from their versatile architectures and topologies as well as their specific potential to form complex structures. For example, the reaction of metal salts with diphosphonate acid creates a cross-linked layered and porous structure. These features indicated their potential as catalysts, sorbants, and ion exchangers.[19,20]

Rare earth(III) phosphonate hybrids are an important family with a potential application in optoelectronic devices. They show unique and interesting luminescence features (e.g., narrow band emission, long lifetime, ligand sensitization, high emission quantum yield, and low toxicity) in the spectral region ranging from the UV to the near-IR.[21–23] The global properties of these luminescent lanthanide (Ln^{3+})-containing hybrids can be well-controlled and tuned by both the inorganic and the organic components. Compared with Ln^{3+} complexes, Ln^{3+}-doped hybrids show a high thermal and photochemical stability and better mechanical properties.[24,25] However, Ln^{3+} complexes are often isolated as hydrates, in which two or three water molecules are included in the first coordination sphere of the central ion. This is undesired, as it leads to a quenching of the emission due to the activation of nonradiative decay paths.[8,26–28]

A further advatage of the use of organophosphorus acid as phosphorus source and organic component of the hybrid structure is that it can be readily modified with several specific functional groups (e.g., −COOH, −NH₂).[29] Such additional functionalities added to the Ln^{3+} phosphonate hybrids can, for example, be used as fluorescent probes in biology with specific optical properties and biocompatibility.[30,31] However, only a few reports on the Ln^{3+}-based phosphonate hybrids are available,

* To whom correspondence should be addressed. E-mail: weihuadi@ua.pt (W.D.), pinna@ua.pt (N.P.), pinna@snu.ac.kr (N.P.).
† Department of Chemistry, CICECO, University of Aveiro.
‡ Chinese Academy of Sciences.
§ Department of Physics, CICECO, University of Aveiro.
‖ Seoul National University.

Rare Earth Phenylphosphonate Hybrid Nanostructures

J. Phys. Chem. C, Vol. 114, No. 14, 2010 **6291**

most of which were focused on the crystal structure determination by X-ray diffraction (XRD) techniques.[30,32] Moreover, the photoluminescence features have been scarcely discussed[33−35] and, to the best of our knowledge, no quantum yield or quantum efficiency values have been reported.

The large majority of the synthesis strategies for metal phosphonate hybrids was carried out by reacting metal salts with phosphonic acid in aqueous solution. The presence of hydroxyl groups in the final material, which is related to the nature of aqueous synthesis, significantly contributes to the quenching of the luminescence properties. It leads to the decrease of the excited-state lifetime value and a reduction of the emission quantum yield of Ln^{3+} through a multiphonon nonradiative relaxation.[8]

Recently, nonaqueous sol−gel routes proved to be generally applicable synthesis strategies for the formation of crystalline metal oxide nanoparticles,[36−38] hybrid materials,[39] and also for the growth of metal oxide thin films by atomic layer deposition.[40]

In this work, we report the nonaqueous synthesis of rare earth phenylphosphonate in which benzyl alcohol was used as solvent. The structure, composition, morphology, thermal and photoluminescence properties were studied in detail. Regarding photoluminescence, emphasis was placed on the role of the ligand in the Ln^{3+} sensitization and on quantitative photoluminescence features, such as the excited-state lifetime, quantum efficiency, and absolute emission quantum yield values. Compared to conventional aqueous routes, the synthesis under nonaqueous conditions contributes to the enhancement of the photoluminescence quantum yield (from 0.25 to 0.45).

Experimental Section

Materials. Phenylphosphonic acid; benzyl alcohol; and anhydrous lanthanum(III), yttrium(III), cerium(III), gadolinium(III), europium(III), and terbium(III) chloride were purchased from Aldrich and used as received without further purification.

Synthesis. The synthesis procedures were carried out in a glovebox (O_2 and H_2O < 1 ppm). In a typical synthesis, 2 mmol of phenylphosphonic acid were dissolved in 15 mL of benzyl alcohol as solvent. Yttrium(III) chloride (1 mmol) (or lanthanum(III), cerium(III), and gadolinium(III) chloride) was added to the above solution, which was then stirred at room temperature for 30 min. After that, the reaction mixtures were transferred into a 23 mL Teflon-lined autoclave. The autoclave was carefully sealed, taken out of the glovebox, and heated in a furnace at 180 °C for 24 h. The resulting milky suspensions were centrifuged, and the precipitates were thoroughly washed with ethanol three times and subsequently dried in air at 50 °C. After these steps, a fine white powder is obtained. For europium(III)- or terbium(III)-doped samples, the synthesis procedure was the same, except that 0.02 or 0.06 mmol of lanthanum(III) or yttrium(III) chloride was replaced by 0.02 or 0.06 mmol of europium(III) chloride or 0.02 mmol of terbium(III) chloride, respectively.

For comparison, hydrothermal synthesis was also carried out to synthesize Ln^{3+} phenylphosphonate hybrids. The conditions were the same as those used in the nonaqueous route, except for replacing the benzyl alcohol by water.

The yield of the products synthesized by benzyl alcohol was about 70−80%, relatively lower than that of aqueous synthesized products (95%).

Measurements. The X-ray powder diffraction (XRD) data were collected on an X'Pert MPD Philips diffractometer (Cu Kα X-radiation at 40 kV and 50 mA). The patterns were measured in the 2θ range from 3.00 to 60.00° with a scanning step of 0.02°.

Transmission electron microscopy (TEM) investigations were carried using a JEOL 2200FS microscope. Samples for TEM investigations were prepared by first dispersing the particles in ethanol under the assistance of ultrasonification and then dropping one drop of the suspension on a copper TEM grid coated with a holey carbon film.

Fourier transform infrared spectroscopy (FT-IR, Mattson 5000) was carried out in the range of 4000−500 cm^{-1} in transmission mode. The pellets were prepared by adding 1−2 mg of the sample powder to 200 mg of KBr. The powders were mixed homogeneously and compressed at a pressure of 10 KPa to form transparent pellets.

Carbon, hydrogen, and nitrogen elemental analyses (CHN) were performed using a CHNS-932 elemental analyzer with standard combustion conditions and handling of the samples in air.

Thermogravimetry and differential thermal analyses (TG and DTA) of the as-synthesized samples were performed with a thermoanalyzer (Netzsch STA 409C/CD). The data were recorded at a scan rate of 10 °C min^{-1} from room temperature to 800 °C under air atmosphere.

The photoluminescence spectra were recorded at room temperature on a Fluorolog-3 model FL3-2T with a double excitation spectrometer and a single emission spectrometer (TRIAX 320) coupled to a R928 photomultiplier, using a front face acquisition mode. The excitation source was a 450 W xenon lamp. Emission was corrected for the spectral response of the monochromators and the detector using a typical correction spectrum provided by the manufacturer, and the excitation spectra were corrected for the spectral distribution of the lamp intensity using a photodiode reference detector. Emission decay curve measurements were carried out at room temperature with the setup described for the luminescence spectra using a pulsed Xe−Hg lamp (6 μs pulse at half width and a 20−30 μs tail).

The absolute emission quantum yields were measured at room temperature using a quantum yield measurement system C9920-02 from Hamamatsu with a 150 W xenon lamp coupled to a monochromator for wavelength discrimination, an integrating sphere as sample chamber, and a multichannel analyzer for signal detection. Three measurements were made for each sample so that the average value is reported. The method is accurate to within 10%.

Results and Discussion

Synthesis and Characterization. The reaction of rare earth(III) chlorides with phenylphosphonic acid in benzyl alcohol results in the formation of lamellar organic−inorganic hybrid materials. All the as-synthesized samples are white powders and were characterized by X-ray diffraction, as shown in Figure 1. The most intense diffraction peak at 5.6° is characteristic of a lamellar structure and corresponds to an interlamellar distance of about 1.55 nm, hence to the (010) reflection of the lamellar structure. Also, the second-, third-, and fourth-order reflections could be clearly assigned at about 11.3, 17.0, and 23.0°, respectively, as indicated in Figure 1a. Among them, the third- and fourth-order reflections overlap with the diffraction peaks characteristic for the inorganic phosphate. The high number of reflections, due to the lamellar periodicity, denotes the high order and the monodispersity in terms of organic and inorganic layer thickness. The other diffraction peaks can be assigned to the inorganic rare earth phosphate layers. The patterns fit well to the structure of lanthanum
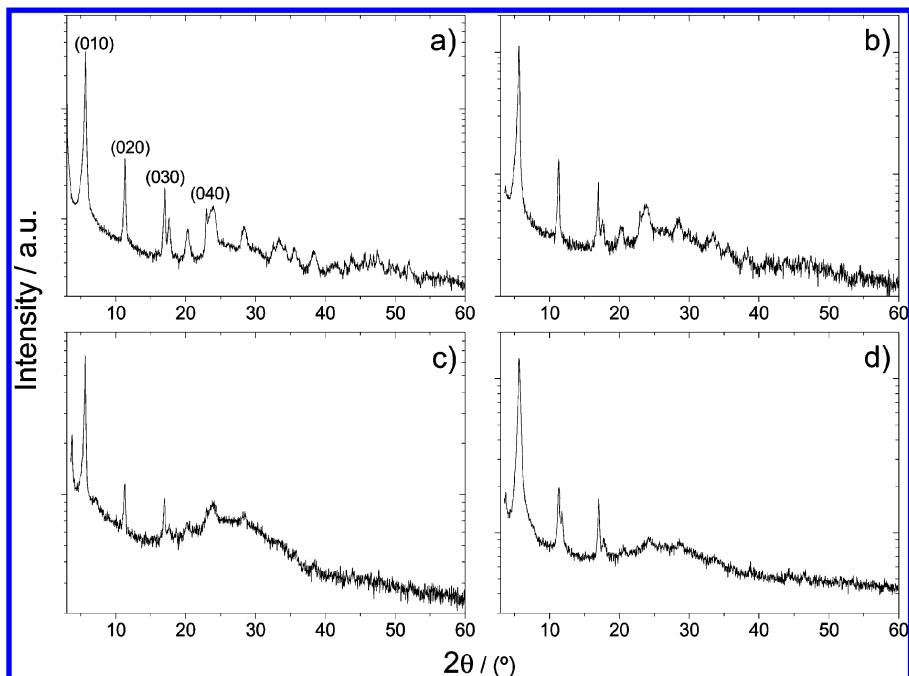
Figure 1. XRD patterns of rare earth phenylphosphonate hybrids synthesized with phenylphosphonic acid as precursor plotted in log scale: (a) $YH(O_3PC_6H_5)_2$, (b) $LaH(O_3PC_6H_5)_2$, (c) $CeH(O_3PC_6H_5)_2$, and (d) $GdH(O_3PC_6H_5)_2$.
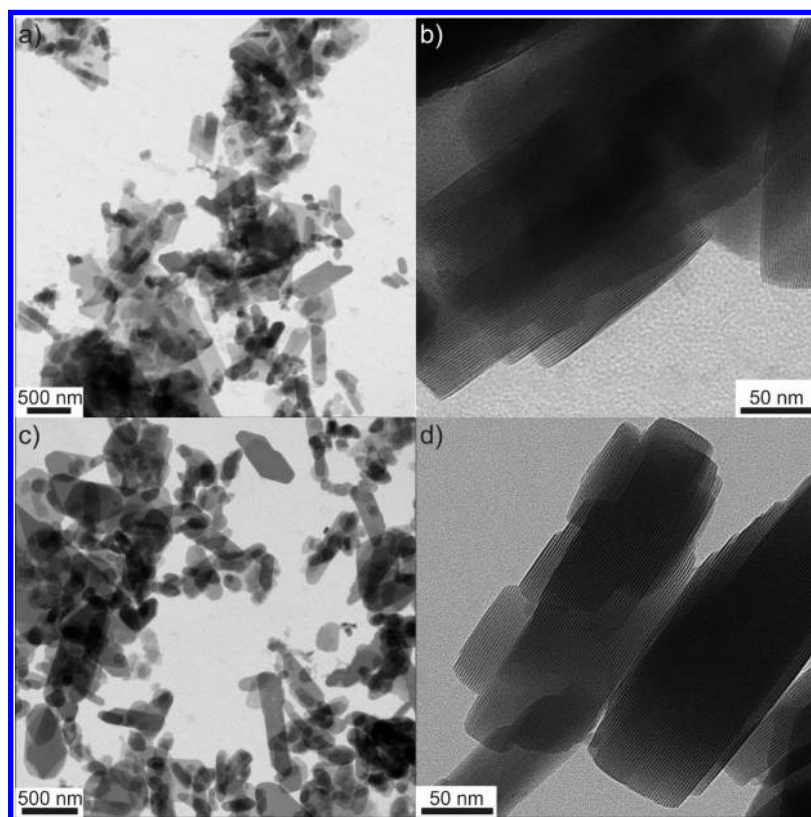
Figure 2. Typical TEM images of rare earth phenylphosphonate hybrids: (a, b) $LaH(O_3PC_6H_5)_2$ and (c, d) $YH(O_3PC_6H_5)_2$.

phenylphosphonate (i.e., $LaH(O_3PC_6H_5)_2$) reported by Clearfield et al.[11] The different rare earth phenylphosphonate hybrids exhibit similar diffraction patterns in the range between 3.00 and 60.00°, indicating that they are characterized by the same interlamellar distance and crystal structure of inorganic layers.

Figure 2 shows the TEM images of representative areas of the as-synthesized nanohybrids. The samples typically consist of nanoparticles and/or nanorods with different particle sizes. The particles are composed of the equally spaced parallel

lamellae with very different electron contrast. The dark layers indicate the presence of the strongest scatterers, corresponding to the inorganic parts, whereas the organic materials stay practically invisible between those layers. The interlayer distance calculated from those pictures was about 1.55 nm, in good agreement with the data obtained by XRD. These findings confirm that the phosphonate bonds (P−C) are stable under the reaction conditions, hence permitting the formation of phenylphosphonate-based hybrids.
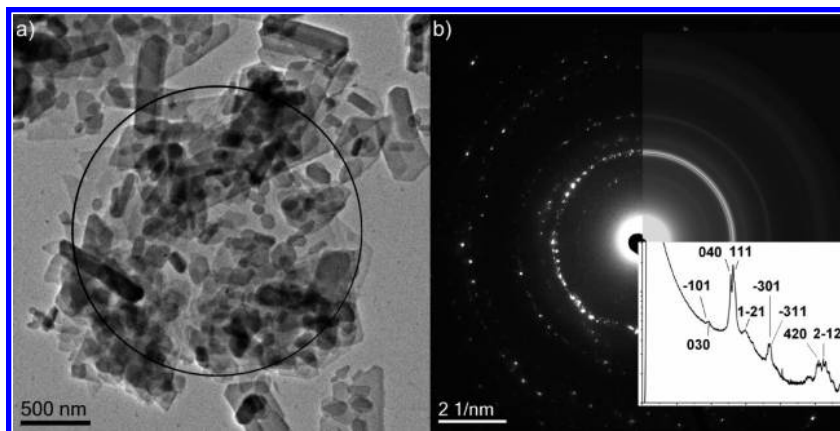
Rare Earth Phenylphosphonate Hybrid Nanostructures

J. Phys. Chem. C, Vol. 114, No. 14, 2010 **6293**

Figure 3. (a) Typical overview TEM image of $YH(O_3PC_6H_5)_2$. The black circle denotes the selected area used for the electron diffraction in (b). In (b), a combination of the electron diffraction, a rotational averaged intensity, and a radial intensity distribution is shown. The most prominent peaks in the intensity plot are labeled according to the corresponding interplanar spacing.

Even though high-resolution TEM images could not be acquired due to the fact that the hybrid material is extremely beam-sensitive, selected area electron diffraction (SAED) recorded in low dose mode could give valuable information about the crystalline structure of the inorganic layers. As the nanoparticles lay principally flat on the carbon-coated TEM grid (i.e., the lamellar periodicity is perpendicular to the plane of the grid) (Figure 3a), the reflections observed in the SAED can be principally attributed to the in-plane crystal periodicity of the inorganic lamellae (Figure 3b). The extracted interplane distances are compared to the ones obtained from XRD measurements and match well with the lanthanum phenylphosphonate $(LaH(O_3PC_6H_5)_2)$ structure reported by Clearfield et al.[11]

CHN elemental analysis gives the content of carbon and hydrogen. The obtained values (31.87% C and 2.76% H for $LaH(O_3PC_6H_5)_2$ and 38.21% C and 3.22% H for $YH(O_3PC_6H_5)_2$,) agree with the values calculated based on the hypothetical chemical formula (31.3% C and 2.24% H for $LaH(O_3PC_6H_5)_2$ and 35.9% C and 2.74% H for $YH(O_3PC_6H_5)_2$).

Figure S1 (Supporting Information) presents the FT-IR absorption spectrum of the lanthanum phenylphosphonate hybrid. The characteristic absorption bands in the 900−1300 cm^{-1} region are due to the different stretching vibrations of the P−O groups. The presence of the bands around 810 and 1315 cm^{-1} is attributed to the P−C stretching vibration. The bands at about 1440 and 1490 cm^{-1} are related to the ν(C=C) vibrations resulting from the aromatic ring. The band at 3052 cm^{-1} is due to the ν(C−H) vibration. These results confirm the formation of the phenylphosphonate organic−inorganic hybrid nanostructure. The low intensity of peaks in the 2922−2995 cm^{-1} region are ascribed to the νs(CH$_2$) and νs(CH$_3$) vibrations resulting from the adsorption of, respectively, solvent (benzyl alcohol) and the ethanol used during the washing procedure, at the surface of the particles. Their presence can explain the slightly higher content of C and H obtained from CHN results as compared to theoretical values for $(La,Y)H(O_3PC_6H_5)_2$. The wide band observed around 3500 cm^{-1} is ascribed to the vibration of O−H due to the H$_2$O adsorbed on the sample surface due to storage in air.

TG and DTA measurements were carried out in order to understand the thermal properties of the as-synthesized nanohybrids. The TG and DTA curves of $LaH(O_3PC_6H_5)_2$ are presented in Figure S2 (Supporting Information). The weight loss occurs in three steps. The first one, at about 120 °C, was associated with the release of 3 wt % of residual water and ethanol adsorbed on the powder surface due to the storage of

the material in air and the washing procedure, respectively. It was accompanied by an endothermic peak at about 120 °C, as shown in the DTA curve. The second weight loss starts at 250 °C and finishes at about 300 °C. It corresponds to the removal of surface-adsorbed benzyl alcohol (∼1 wt %), which is known to desorb above 200 °C.[41] This is also accompanied by an endothermic peak with low intensity centered at 280 °C. The most significant weight loss was observed between 400 and 500 °C. It is attributed to the decomposition of the hybrid structure and the burning of the organic moieties. Indeed, an exothermic peak centered at 500 °C is observed in the DTA curve. A weight loss of 26% associated with the decomposition of the hybrid structure is observed. This agrees well with the C and H content obtained from CHN analysis and the empirical formula of $LaH(O_3PC_6H_5)_2$. Yttrium and gadolinium phosphonate nanohybrids exhibit similar thermal properties to those of $LaH(O_3PC_6H_5)_2$ (not shown). TG measurements indicate a high thermal stability of phenylphosphonate-based hybrids, which is astonishing because the hybrid lamellar structure is kept together only by $\pi-\pi$ interactions between the phenyl rings.

Photoluminescence Properties. Figure 4A shows the excitation spectrum monitored within the $^5D_0 \rightarrow {}^7F_2$ transition (612 nm) of Eu^{3+} for the $LaH(O_3PC_6H_5)_2$:0.06Eu nanohybrid and Figure S3 (Supporting Information) shows the respective UV−vis absorption spectrum.

The spectrum consists of a broad band peaking at 276 nm ascribed to the excited states of the phenyl rings coordinated to the Eu^{3+} ions[34,35] and of a shoulder at ∼268 nm attributed to a ligand-to-metal charge transfer (LMCT) band associated with the excitation of an electron from the 2p oxygen orbital to the 4f^6 orbital.[45] The high-wavelength region (300−550 nm) shows a series of lines ascribed to intra-4f^6 transitions between the $^7F_{0,1}$ levels and the $^5H_6$, $^5D_{4-1}$, $^5G_{2-6}$, and $^5L_6$ excited states. The relatively high intensity of the broad band points out that the Eu^{3+} ions are essentially populated via the excitation of the phenyl rings' excited states.

The excitation spectrum of $LaH(O_3PC_6H_5)_2$:0.02Tb was also acquired at 300 K by monitoring within the $^5D_4 \rightarrow {}^7F_5$ transition (544 nm) (Figure 4B). The spectrum displays a main large broad band peaking at 276 nm assigned to the phenyl excited states and a series of intra-4f^8 lines attributed to transitions between the $^7F_6$ level and the $^5L_{10-7}$, $^5G_{6-2}$, and $^5D_{4,2}$ excited states. They are superimposed on the broad band (400−600 nm) originating from the excited states of the phenyl groups whose emitting levels overlap with the Tb^{3+} excited states. Thus, the excitation spectrum in Figure 4B shows the excitation contributions of
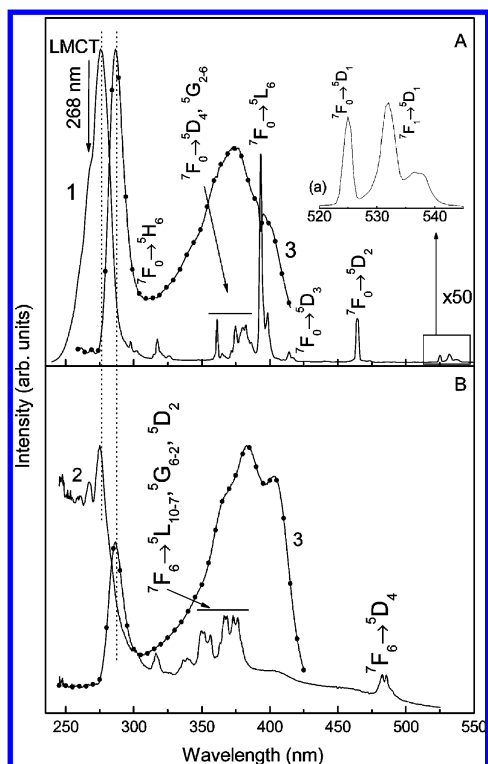
Figure 4. Excitation spectra of (A) $LaH(O_3PC_6H_5)_2$:0.06Eu and (B) $LaH(O_3PC_6H_5)_2$:0.02Tb nanohybrids monitored at (1) 612, (2) 544, and (3) 450 nm. The inset shows a magnification of the $^7F_{0,1} \rightarrow {}^5D_1$ transitions.

both emissions. The components in the low-wavelength region, discerned at ~240 and 280 nm, can be related to the spin-forbidden (low-spin, LS, and high-spin, HS) interconfigurational fd transitions, respectively.[42–44] Similar to that found for the Eu^{3+}-doped nanohybrids, the main intra-4f excitation path proceeds via the phenyl ring excited states.

Figure 5A displays the emission features of the $LaH(O_3PC_6H_5)_2$:0.06Eu nanohybrid under distinct excitation wavelengths. For excitation wavelengths between 250 and 280 nm, the spectra display essentially the $^5D_0 \rightarrow {}^7F_{0-4}$ transitions, whereas for higher excitation wavelengths (300–405 nm), the intra-4f^6 lines are superimposed on the broad band (400–600 nm) originating from the excited states of the phenyl groups,[45,46] as we detail below. A self-absorption ascribed to the $^7F_0 \rightarrow {}^5D_2$ transition is also detected, as denoted by the asterisk symbols. The relative intensity between the phenyl-related band and the intra-4f^6 transitions depends on the Eu^{3+} concentration (not shown) in such a way that increasing the amount of Eu^{3+} leads to a decrease of the broad-band emission of the phenyl rings, which is in good agreement with the presence of ligand(phenyl)-to-Eu^{3+} energy transfer.

The emission features of $LaH(O_3PC_6H_5)_2$:0.02Tb are shown in Figure 5B. The spectra display the phenyl-related emission superimposed on the $^5D_4 \rightarrow {}^7F_{6-3}$ transitions of Tb^{3+}. Contrary to what was found for the Eu^{3+}-doped hybrids, the phenyl-related emission band is observed in the entire excitation wavelength range (250–405 nm), pointing out a less efficient ligands-to-Tb^{3+} energy transfer, when compared with that in the case of the Eu^{3+}-based materials. To interpret the distinct relative intensity dependence of the phenyl rings' broad band in the case of the Eu^{3+}- and Tb^{3+}-doped samples, we plot the energy level diagram, showing the intra-4f levels and the triplet state of the phenyl rings (Figure 5C). The energy and width of the phenyl rings' triplet state was estimated from the peak

position and fwhm of the emission spectra, respectively. As shown in Figure 5C, there is a great overlap between the phenyl rings' triplet state and the intra-4f^6 levels of Eu^{3+}, relative to that involving the intra-4f^8 states of Tb^{3+}. Moreover, the triplet state energy is resonant with the $^5D_4$ level, favoring a higher contribution from $Tb^{3+}(^5D_4)$-to-ligand(T) energy back-transfer. In this context, for the Tb^{3+}-doped hybrids, the triplet state emission occurs simultaneously to that arising from the intra-4f^8 levels.

The photoluminescence features of the phenyl-related broad band were further studied through the measurement of the excitation spectra along the emission spectra (400–600 nm) for both the Eu^{3+}- and the Tb^{3+}-doped nanohybrids. The energy of the excitation spectra is independent of the monitoring wavelength. Figure 4A and 4B shows the excitation spectra monitored around the broad-band peak position, revealing a component at 284 nm and another broader component peaking at 375 nm. The component at 284 nm is slightly red shifted compared with that found in the excitation spectra monitored within the intra-4f lines. We tentatively assigned these two components to the emission of phenyl rings of the phenylphosphonate complexes that are not coordinated to Eu^{3+} and Tb^{3+} ions (i.e., they are coordinated to La^{3+} or Y^{3+} only).[45]

To acquire additional information on the Eu^{3+} local environment, high-resolution emission spectra of $LaH(O_3PC_6H_5)_2$:0.06Eu were measured (Figure 6). The energy, fwhm, and number of Stark components of the Eu^{3+} emission lines are independent of the excitation path (direct intra-4f^6 excitation or via the phenyl-related states), suggesting that all the Eu^{3+} ions occupy the same average local environment characterized by a local-symmetry group without an inversion center, in accordance with the relatively high intensity of the $^5D_0 \rightarrow {}^7F_2$ transition. Moreover, the presence of a single component for the $^5D_0 \rightarrow {}^7F_0$ transition, which occurs between nondegenerate states, reinforces the presence of a single local environment for the Eu^{3+} ions, in agreement with the single-crystal structure of the phenylphosphonate hybrid reported by Clearfield et al.[11] The energy, fwhm, and number of Stark components are independent of the Eu^{3+} concentration (not shown), indicating the same Eu^{3+} local coordination site for all the hybrids.

The photoluminescence features were quantified through the estimation of the absolute emission quantum yield as a function of the Ln^{3+} concentration in the presence of Y or La. For the Tb^{3+}-doped hybrids, a maximum quantum yield value was obtained under 360 nm excitation wavelength, being 0.23 and 0.08 for the $YH(O_3PC_6H_5)_2$:0.02Tb and $LaH(O_3PC_6H_5)_2$:0.02Tb, respectively. The higher quantum yield value found for the Y-based hybrids points out the presence of a lower $^5D_4$ nonradiative transition probability in these materials with respect to the La-containing ones.

For the Eu^{3+}-containing materials, the highest quantum yield value (0.45) was obtained for $LaH(O_3PC_6H_5)_2$:0.06Eu upon 275 nm excitation. For the lower concentrated sample $LaH(O_3PC_6H_5)_2$:0.02Eu, a reduction of the quantum yield value to 0.36 is observed. For the Y-based materials, which have approximately the same value independent of the Eu^{3+} concentration (cf. Table 2), lower values were obtained relative to those of the La-containing hybrids. We should note that the quantum yield values reported here are substantially higher than those reported for Eu^{3+}-doped Gd_2O_3 benzoate-based hybrids synthesized using a similar nonaqueous route (0.16 ± 0.02).[46]

To further investigate the role of the nonaqueous synthesis route on the enhancement of the Eu^{3+} optical features, the photoluminescence features and the absolute emission quantum
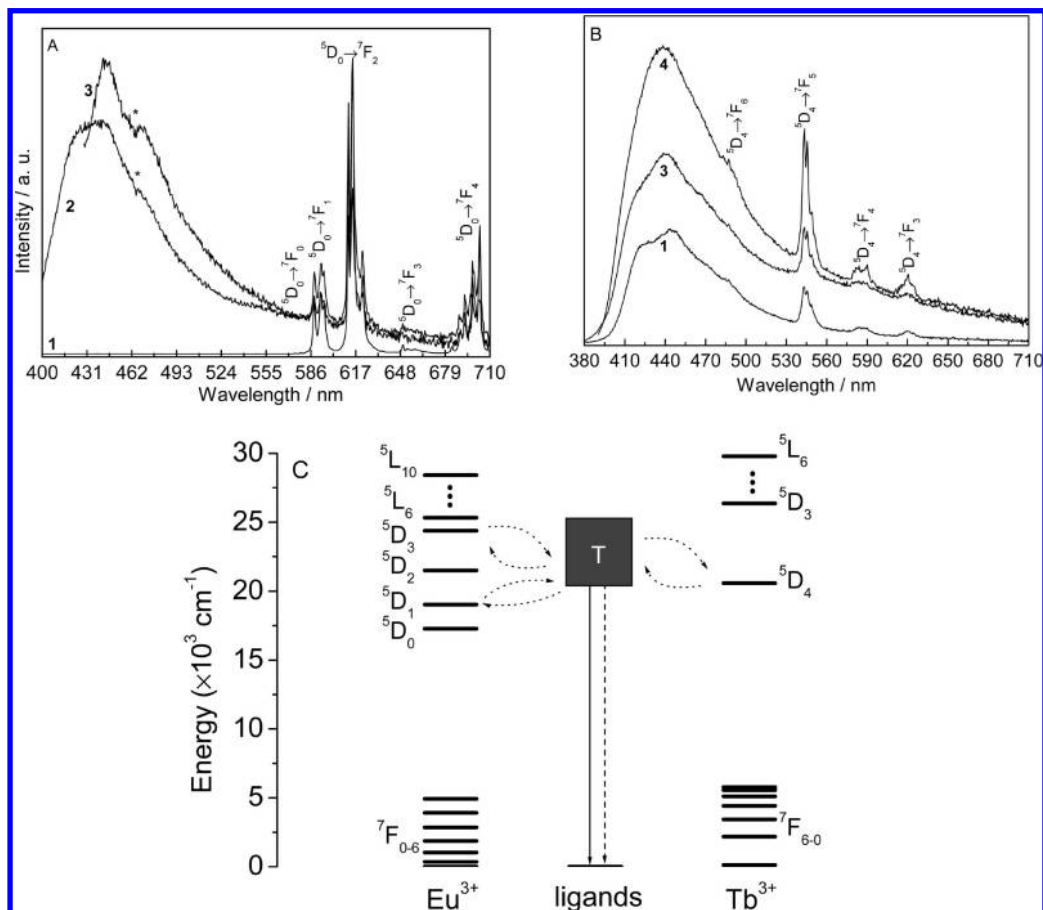
Rare Earth Phenylphosphonate Hybrid Nanostructures

J. Phys. Chem. C, Vol. 114, No. 14, 2010 **6295**

Figure 5. Emission spectra of (A) LaH(O$_3$PC$_6$H$_5$)$_2$:0.06Eu and (B) LaH(O$_3$PC$_6$H$_5$)$_2$:0.02Tb excited at (1) 287, (2) 370, (3) 405, and (4) 360 nm. The asterisk denotes the intra-4f^6 ^{7}F$_0$ → ^{5}D$_2$ self-absorption of Eu^{3+}. (C) Partial scheme of the energy levels of the Eu^{3+} (intra-4f^6) and Tb^{3+} (intra-4f^8) and of the triplet state (T) from the phenyl ligands. The straight solid and dashed arrows represent, respectively, radiative and nonradiative transitions from the phenyl ring levels. Some possible energy transfer paths between them and the intra-4f levels are identified by the curved dotted lines.
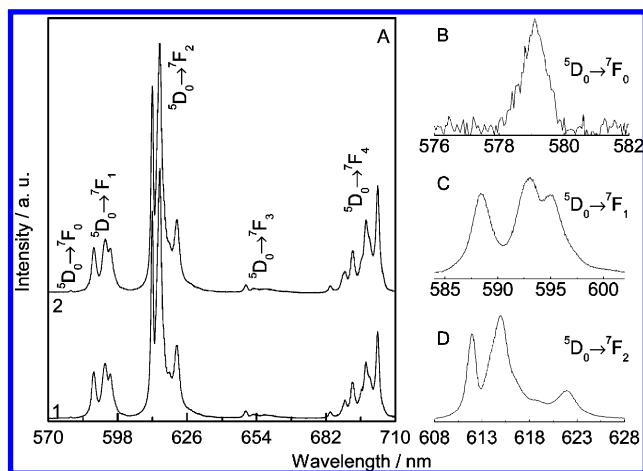

Figure 6. (A) High-resolution emission spectra of the LaH(O$_3$PC$_6$H$_5$)$_2$:0.06Eu excited at (1) 286 and (2) 393 nm. (B−D) Magnification of the ^{5}D$_0$ → ^{7}F$_{0-2}$ transitions excited at 393 nm.

yield of Eu^{3+} nanohybrids prepared under hydrothermal conditions and with the same Eu^{3+} amount were estimated under the same experimental conditions. When the emission features of the hydrothermally synthesized La(HO$_3$PC$_6$H$_5$)$_2$:0.06Eu hybrid are compared with that of La(HO$_3$PC$_6$H$_5$)$_2$:0.06Eu synthesized in benzyl alcohol, changes are observed in the energy of the Stark components, pointing to changes in the Eu^{3+} local environment (Figure S4 of the Supporting Information). For the hydrothermally synthesized La(HO$_3$PC$_6$H$_5$)$_2$:0.06Eu material,

TABLE 1: Absolute Emission Quantum Yield (ϕ)^a for La(HO$_3$PC$_6$H$_5$)$_2$:0.06Eu Synthesized in Benzyl Alcohol (Nonaqueous) and under Hydrothermal Conditions (Aqueous) for Various Excitation Wavelengths

excitation (nm)	275	286	370	393	405
ϕ nonaqueous	0.45	0.37	0.17	0.16	0.07
ϕ aqueous	0.25	0.19	0.10	0.10	0.04

^{a} The experimental error is within 10%.

lower quantum yield of 0.25 was measured (excited at 275 nm), suggesting that the nonaqueous approach is a more suitable way to obtain materials with higher luminescence efficiency. Table 1 summarizes the variation of the quantum yield values as a function of the excitation wavelength. The quantum yield decreases progressively with the increase of the excitation wavelength for both La(HO$_3$PC$_6$H$_5$)$_2$:0.06Eu materials. This can be explained by the fact that the probability of transfer between organic ligands and the intra-4f^8 energy levels of Eu^{3+} decreases with the increase of excitation wavelength. It is important to note that the same material synthesized in benzyl alcohol always presents quantum yield values almost twice as large as the one synthesized under hydrothermal conditions.

The photoluminescent features of the hybrids prepared under nonaqueous conditions were further quantified through the estimation of the ^{5}D$_0$ (Eu^{3+}) and ^{5}D$_4$ (Tb^{3+}) lifetime values. The emission decay curves were monitored at 612 nm (^{5}D$_0$ → ^{7}F$_2$) and 544 nm (^{5}D$_4$ → ^{7}F$_5$), under excitation at ∼274

TABLE 2: Lifetime (τ, ms), Quantum Efficiency (η), Radiative (k_r, ms^{-1}) and Nonradiative (k_{nr}, ms^{-1}) Transition Probability Values of the $^5D_0$ Level, Number of Water Molecules Coordinated to the Eu^{3+} Ion ($n_w \pm 0.1$), and Absolute Emission Quantum Yield (ϕ)^a for $Y(HO_3PC_6H_5)_2$:0.02Eu and $Y(HO_3PC_6H_5)_2$:0.06Eu

	$Y(HO_3PC_6H_5)_2$	
	0.02% Eu	0.06% Eu
τ	2.416 ± 0.006	1.742 ± 0.002
k_r	0.255	0.241
k_{nr}	0.159	0.333
η	0.62	0.42
n_w	0.0	0.0
ϕ	0.32	0.31

^{a} The experimental error is 10%.

nm for all the nanohybrids. All the decay curves reveal a single exponential behavior (not shown), in good agreement with the presence of a single average local environment for the Ln^{3+} ions within each sample. For the Tb^{3+}-doped hybrids, $^5D_4$ lifetime values of 2.015 ± 0.014 and 1.823 ± 0.020 ms were estimated for $Y(HO_3PC_6H_5)_2$:0.02Tb and $La(HO_3PC_6H_5)_2$:0.02Tb, respectively. This $^5D_4$ lifetime value variation suggests a higher contribution of nonradiative channels in the La-based nanohybrid, which may be responsible for the lower quantum yield values found for these hybrids with respect to the ones of the Y-based nanohybrids (see above).

The $^5D_0$ emission decay curves are also well-described by a single exponential function, yielding lifetime values of 2.416 ± 0.006 and 1.742 ± 0.002 ms for $Y(HO_3PC_6H_5)_2$:0.02/0.06Eu (Table 2) and 2.325 ± 0.001 and 1.717 ± 0.003 ms for $La(HO_3PC_6H_5)_2$:0.02/0.06Eu. For the same Ln^{3+} concentration, contrary to that found for the Tb^{3+}-doped materials, the $^5D_0$ lifetime values display a minor variation (<5%) in the presence of La or Y. Furthermore, these values are higher than those reported for Eu^{3+} organophosphonates prepared by aqueous routes, suggesting that the nonaqueous synthesis route may also contribute to the enhancement of the Eu^{3+} photoluminescence features.[35]

To further interpret the variations in $^5D_0$ lifetime as the Eu^{3+} amount increases from 0.02 to 0.06%, the radiative (k_r) and nonradiative (k_{nr}) transition probabilities of the $^5D_0$ level and the quantum efficiency (η), $\eta = k_r/(k_r + k_{nr})$, were estimated for the $Y(HO_3PC_6H_5)_2$:0.02/0.06Eu hybrids, using a procedure based on the room-temperature emission spectrum and $^5D_0$ lifetime values.[8] The radiative contribution may be calculated from the relative intensities of the $^5D_0 \rightarrow {}^7F_{0-4}$ transitions (the $^5D_0 \rightarrow {}^7F_{5,6}$ branching ratios are neglected due to their poor relative intensity with respect to that of the remaining $^5D_0 \rightarrow {}^7F_{0-4}$ lines). The $^5D_0 \rightarrow {}^7F_1$ transition does not depend on the local ligand field and thus may be used as a reference for the whole spectrum; in vacuum $A_{0-1} = 14.65$ s^{-1}.[47] An effective refractive index of 1.5 was used, leading to $A(^5D_0 \rightarrow {}^7F_1) \approx 50$ s^{-1}. The values found for η, k_r, and k_{nr} are gathered in Table 2.

The quantum efficiency value depends on the Eu^{3+} amount being higher for the less concentrated samples, $Y(HO_3PC_6H_5)_2$:0.02Eu ($\eta = 0.62$) essentially due to a smaller k_{nr} value (0.52) when compared with that of the $Y(HO_3PC_6H_5)_2$:0.06Eu ($\eta = 0.42$).

The k_{nr} value may be related with the number of water molecules ($n_w \pm 0.1$) in the Eu^{3+} first coordination shell, through the empirical formula $n_w = 1.11 \times [\tau^{-1} - k_r - 0.31]$[8,48] (Table 2). The n_w values calculated for the hybrids point to the absence of water molecules coordinated to the Eu^{3+} ions. This certainly plays a key role in the enhancement of the emission quantum yield values discussed in this work compared with similar nanohybrids.[34,45,49]

Conclusions

A novel nonaqueous route was introduced for the synthesis of hybrid rare earth phenylphosphonates by reacting rare earth chlorides with phenylphosphonic acid in benzyl alcohol. The reaction results in the formation of ordered lamellar organic−inorganic hybrid nanoparticles made of rare earth phosphate layers separated by phenyl rings. The emission spectra of the Ln^{3+}-doped hybrids exhibit a large broad band (380−650 nm), ascribed to the phenyl-related states, and a series of narrow lines ascribed to the Eu^{3+} $^5D_0 \rightarrow {}^7F_{0-4}$ and Tb^{3+} $^5D_4 \rightarrow {}^7F_{6-3}$ intra-4f transitions. The broad-band relative intensity strongly depends on the amount of Ln^{3+} incorporated and on the excitation wavelength, in agreement with the active ligands-to-Ln^{3+} energy transfer path. The Eu^{3+} ions were used as local structural probes. The detection of a single $^5D_0 \rightarrow {}^7F_0$ line, the J-degeneracy splitting of the $^7F_{1,2}$ levels into three and five Stark components, the observation of this same number of local-field split components over the entire range of excitation wavelength used, and the fact that the $^5D_0$ (Eu^{3+}) is well-modeled by a single exponential function indicate the same average local environment for the Ln^{3+} cations in each hybrid. The Eu^{3+} ions occupy a low symmetry site, without an inversion center, in accordance with the higher intensity of the electric-dipole $^5D_0 \rightarrow {}^7F_2$ transition, relative to that of the magnetic-dipole $^5D_0 \rightarrow {}^7F_1$ one. The $^5D_0$ lifetime and quantum efficiency values were estimated, revealing maximum values of ∼2.416 ms and 0.62, respectively. The emission features were also quantified through the measurement of the absolute emission quantum yield, whose maximum value (0.45) was acquired under excitation via the phenyl excited states, being significantly higher than the value measured (0.25) for analogous materials prepared via an aqueous route. The ultimate goal of this investigation was to elucidate the role of the synthesis route on the photoluminescent features. This work demonstrated that nonaqueous approaches open new prospects for the design of high-quality luminescent materials.

Supporting Information Available: FT-IR spectra, TG and DTA curves, and UV−vis absorption and high-resolution emission spectra of Eu-doped samples. This material is available free of charge via the Internet at http://pubs.acs.org.

References and Notes

(1) Brinker, C. J.; Scherer, G. W. *Sol-Gel Science: The Physics and Chemistry of Sol-Gel Processing*; Academic Press: San Diego, CA,1990.
(2) Schmidt, H. *J. Sol−Gel Sci. Technol.* **2006**, *40*, 115.
(3) Avnir, D. *Acc. Chem. Res.* **1995**, *28*, 328.
(4) Corriu, R.; Leclercq, D. *Angew. Chem., Int. Ed. Engl.* **1996**, *35*, 1420.
(5) Li, H.; Liu, P.; Wang, Y.; Zhang, L.; Yu, J.; Zhang, H.; Liu, B.; Schubert, U. *J. Phys. Chem. C* **2009**, *113*, 3945.
(6) Sanchez, C.; Ribot, F. *New J. Chem.* **1994**, *18*, 1007.
(7) Judeinstein, P.; Sanchez, C. *J. Mater. Chem.* **1996**, *6*, 511.
(8) Carlos, L. D.; Ferreira, R. A. S.; de Zea Bermudez, V.; Ribeiro, S. J. L. *Adv. Mater.* **2009**, *21*, 509.

(9) Sanchez, C.; Lebeau, B.; Chaput, F.; Boilot, J. P. *Adv. Mater.* **2003**, *15*, 1969.

(10) Sanchez, C.; Soler-Illia, G.; Ribot, F.; Lalot, T.; Mayer, C. R.; Cabuil, V. *Chem. Mater.* **2001**, *13*, 3061.

(11) Wang, R.; Zhang, Y.; Hu, H.; Rrausto, R.; Clearfield, A. *Chem. Mater.* **1992**, *4*, 864.

(12) Cabeza, A.; Aranda, M.; Bruque, S.; Poojary, D.; Clearfield, A.; Sanz, J. *Inorg. Chem.* **1998**, *37*, 4168.

(13) Yim, C.; Pawsey, S.; Morin, E.; Reven, L. *J. Phys. Chem. B* **2002**, *106*, 1728.

(14) Johnson, J. W.; Jacobson, A. J.; Brody, J. F.; Lewandowski, J. T. *Inorg. Chem.* **1984**, *23*, 3842.

(15) Alberti, G.; Constantino, U.; Kornyei, J.; Luciani, M. L. *React. Polym.* **1985**, *4*, 1.

(16) Yang, C.; Clearfield, A. *React. Polym.* **1987**, *5*, 13.

(17) Cao, G.; Lee, H.; Lynch, V. M.; Mallouk, T. E. *Inorg. Chem.* **1988**, *26*, 63.

(18) Martin, K. J.; Squattrito, P. J.; Clearfield, A. *Inorg. Chim. Acta* **1989**, *155*, 7.

(19) Clearfield, A. *Design of New Materials*; Plenum Press: New York, 1986.

(20) Ma, T.; Zhang, X.; Shao, G.; Cao, J.; Yuan, Z. *J. Phys. Chem. C* **2008**, *112*, 3090.

(21) Guo, Y. Q.; Tang, S. F.; Yang, B. P.; Mao, J. G. *J. Solid State Chem.* **2008**, *181*, 2713.

(22) Liu, F. Y.; Roces, L.; Ferreira, R. A. S.; Garcia-Granda, S.; Garcia, J. R.; Carlos, L. D.; Rocha, J. *J. Mater. Chem.* **2007**, *17*, 3696.

(23) Gameiro, C. G.; da Silva, E. F.; Alves, S.; de Sa, G. F.; Santa-Cruz, P. A. *J. Alloys Compd.* **2001**, *323−324*, 820.

(24) Lima, P. P.; Ferreira, R. A. S.; Freire, R. O.; Paz, F. A. A.; Fu, L. S.; Alves, S., Jr.; Carlos, L. D.; Malta, O. L. *ChemPhysChem* **2006**, *7*, 735.

(25) Pagnot, T.; Audebert, P.; Tribillon, G. *Chem. Phys. Lett.* **2000**, *322*, 572.

(26) Binnemans, K. *Handbook on the Physics and Chemistry of Rare Earths*; Elsevier: Amsterdam, The Netherlands, 2005; pp 107−272.

(27) Gawryszewska, P.; Sokolnicki, J.; Legendziewicz, J. *Coord. Chem. Rev.* **2005**, *249*, 2489.

(28) Sun, L.; Zhang, H.; Meng, Q.; Liu, F.; Fu, L.; Peng, C.; Yu, J.; Zheng, G.; Wang, S. *J. Phys. Chem. B* **2005**, *109*, 6174.

(29) Sun, L.-N.; Zhang, H.-J.; Peng, C.-Y.; Yu, J.-B.; Meng, Q.-G.; Fu, L.-S.; Liu, F.-Y.; Guo, X.-M. *J. Phys. Chem. B* **2006**, *110*, 7249.

(30) Ying, S. M.; Mao, J. G. *Cryst. Growth Des.* **2006**, *6*, 964.

(31) Mao, J. G. *Coord. Chem. Rev.* **2007**, *251*, 1493.

(32) Alsobrook, A. N.; Zhan, W.; Albrecht-Schmitt, T. E. *Inorg. Chem.* **2008**, *47*, 5177.

(33) Song, S. Y.; Ma, J. F.; Cao, M. H.; Zhang, H. J.; Wang, H. S.; Yang, K. Y. *Inorg. Chem.* **2006**, *45*, 1201.

(34) Rosa, I. L. V.; Nassar, E. J.; Serra, O. A. *J. Alloys Compd.* **1998**, *275−277*, 315.

(35) Rosa, I. L. V.; Lourenco, A. V. S.; Neri, C. R. *J. Fluoresc.* **2006**, *16*, 455.

(36) Pinna, N.; Niederberger, M. *Angew. Chem., Int. Ed.* **2008**, *47*, 5292.

(37) Niederberger, M. *Acc. Chem. Res.* **2007**, *40*, 793.

(38) Mutin, P. H.; Vioux, A. *Chem. Mater.* **2009**, *21*, 582.

(39) Pinna, N. *J. Mater. Chem.* **2007**, *17*, 2769.

(40) Clavel, G.; Rauwel, E.; Willinger, M.-G.; Pinna, N. *J. Mater. Chem* **2009**, *19*, 454.

(41) Niederberger, M.; Garnweitner, G.; Krumeich, F.; Nesper, R.; Colfen, H.; Antonietti, M. *Chem. Mater.* **2004**, *16*, 1202.

(42) Laroche, M.; Doualan, J. L.; Girard, S.; Margerie, J.; Moncorgé, R. J. *J. Opt. Soc. Am. B* **2000**, *17*, 1291.

(43) van Pierterson, L.; Reid, M. F.; Burdick, G. W.; Meijerink, A. *Phys. Rev. B* **2002**, *65*, 045114.

(44) Di, W. H.; Willinger, M.-G.; Ferreira, R. A. S.; Ren, X. G.; Lu, S. Z.; Pinna, N. *J. Phys. Chem. C* **2008**, *112*, 18815.

(45) Ferreira, R. A. S.; Karmaoui, M.; Nobre, S. S.; Carlos, L. D.; Pinna, N. *ChemPhysChem* **2006**, *7*, 2215.

(46) Karmaoui, M.; Ferreira, R. A. S.; Mane, A. T.; Carlos, L. D.; Pinna, N. *Chem. Mater.* **2006**, *18*, 4493.

(47) Werts, M. H. V.; Jukes, R. T. F.; Verhoeven, J. W. *Phys. Chem. Chem. Phys.* **2002**, *4*, 1542.

(48) Supkowski, R. M.; Horrocks, W. D. *Inorg. Chim. Acta* **2002**, *340*, 44.

(49) Ferreira, R. A. S.; Carlos, L. D.; Goncalves, R. R.; Ribeiro, S. J. L. *Chem. Mater.* **2001**, *13*, 2991.